

KELVIN-HELMHOLTZ INSTABILITIES  
OF HIGH-VELOCITY MAGNETIZED SHEAR LAYERS  
WITH GENERALIZED POLYTROPE LAWS

BY

KEVIN G. BROWN AND S. ROY CHOUDHURY

*Department of Mathematics, University of Central Florida, Orlando, FL*

**Abstract.** The linear stability of zero and finite width, arbitrarily compressible, and magnetized velocity shear layers with isotropic or anisotropic pressure is investigated. Such flows, modeled by the magnetohydrodynamic equations with generalized polytrope laws for the pressure parallel and perpendicular to the magnetic field, are relevant in various astrophysical, geophysical and space plasma configurations. The conditions for instability of shear layers of zero width are derived. For layers of finite width, shooting numerical schemes are employed to satisfy the Sommerfeld radiation conditions of outgoing, spatially damping modes in a frame comoving with the plasma flow. The resulting eigenvalues for the angular frequency and linear growth rate are mapped out for different regions of the wave number/Mach number space. For polytrope indices corresponding to the double adiabatic and magnetohydrodynamic equations, the results reduce to those obtained earlier using these models.

**1. Introduction.** The Kelvin-Helmholtz (K-H) instability caused by tangential velocity discontinuities in homogeneous plasma is of crucial interest in understanding the problems of space, astrophysical and geophysical situations involving sheared plasma flows. A detailed understanding of the structure and dynamics of magnetopause regions, such as the presence of the magnetospheric boundary layer and of rapid boundary motions has been obtained from the recent satellite observations of particles and fields. Many workers have discussed the instability of the interface between the solar wind and the magnetosphere [1]–[5], coronal streamers moving through the solar wind, the boundaries between the adjacent sectors in the solar wind, the structure of the tails of comets [6], [7], and the boundaries of the jets propagating from the nuclei of extragalactic double radio sources into their lobes [8]–[9]. The linear K-H instability of nonmagnetized shear layers has been studied for flows with subsonic velocity change by Chandrasekhar, Syrovatskii, and Northrop [10], and with an abrupt jump in  $v_z$  of arbitrary magnitude

Received February 24, 1997.

2000 *Mathematics Subject Classification.* Primary 76Exx, 76J20, 76W05, 35Qxx.

*E-mail address:* choudhur@longwood.cs.ucf.edu

by Gerwin [11]. Ray and Ershkovich [12], and Miura [13] have discussed the stability of compressible, magnetized, finite-width shear layers for a linear and hyperbolic tangent velocity profile. The K-H instability of a finite-width, ideal magnetohydrodynamic shear layer with linear and hyperbolic tangent velocity profiles in the transition region has been discussed by Roy Choudhury and Lovelace, and Miura and Pritchett [14] and by Roy Choudhury [15] considering arbitrary magnetic fields in the  $(y, z)$ -plane. Uberoi [16] has investigated the finite thickness and angle effects on the marginal instability considering the three-layered structure of plasma regions; the magnetosheath, the boundary layer, and the magnetosphere. Fujimoto and Terasawa [17] have carried out the study of the ion inertia effect on the K-H instability of two-fluids plasma arising from the Hall term. Sharma and Shrivastava [18] have presented the nonlinear analysis of drift K-H instability for electrostatic perturbations. Malik and Singh [19] have studied chaos in the K-H instability in superposed magnetic fluids with uniform relative motion.

In the above studies, most of the treatments used the collision-dominated hydromagnetic equations with scalar gas pressure approximation. The scalar gas pressure approximation is not appropriate in dilute plasmas such as the coronal streamers and the solar wind. The plasma in the interplanetary medium, earth's magnetosphere and the polar exosphere are collisionless. There is a transition zone in solar wind where plasma is neither fully collisional nor collisionless. The K-H instability has been discussed in anisotropic plasma using Chew, Goldberger, and Low (CGL) equations for the situations where collisions are not sufficiently strong to keep the pressure a scalar but sufficiently strong to prevent the heat flow and other transport processes. Roy Choudhury and Patel [20] have considered the K-H instability of an anisotropic, finite-width, supersonic shear layer and investigated the nonlocal coupling of the firehose and mirror instabilities via a spatially varying velocity. Duhau et al. [21], [22] have discussed the problem of a tangential velocity discontinuity in a collisionless hydromagnetic region using CGL approximation. Duhau and Gratton [23] have investigated the effect of compressibility on the stability of a vortex sheet in an ideal magnetofluid. Rajaram et al. [24], [25] have examined the contact discontinuities on two collisionless fluids in the magnetosphere across the cusp region of the solar wind magnetosphere boundary. Talwar [26], [27] has presented a study of K-H instability of two streams of homogeneous anisotropic plasma. Pu [28] has developed a new approach called the drift kinetic approximation (DKA) for collisionless space plasmas.

However, more general anisotropic models than the CGL model are necessary in treating low-collision regimes, such as in the transitional region of the solar wind. In this connection, we employ the plasma model with generalized polytropic laws for the parallel and perpendicular pressures. This model, proposed by Abraham Shrauner [29], uses double adiabatic pressure laws with generalized polytropic indices together with the other magnetohydrodynamic (MHD) equations. For specific choices of polytropic indices, it contains both the MHD and CGL models as special cases. In this paper, we consider the K-H instability of a finite-width velocity shear layer with arbitrary compressibility and a linear velocity profile using this model. The governing equations are very complicated and their solution involves the use of a general shooting procedure to satisfy the Sommerfeld radiation conditions [14] of outgoing, spatially damping solutions in a frame

comoving with the plasma. The resulting values of the angular frequency and growth rate of the linear perturbation field are mapped out in the wave number/Mach number plane. These results are compared to those obtained earlier using the MHD and CGL models. Specific applications of these results are not considered here, but will be treated in a future, more physics-oriented, report. The objective here is to treat the mathematical aspects of the generalized K-H instability using this most general formulation, which contains all previous results as special cases.

The remainder of this paper is organized as follows. Sections 2 and 3 describe the governing equations and the external solutions in the regions outside the region of velocity shear. The instability of zero-width shear layers is considered in Sec. 4. Section 5 details the numerical technique for satisfying the boundary conditions for shear regions of finite width. Finally, the results and conclusions are presented in Sec. 6.

**2. Anisotropic plasma equations with generalized polytrope laws.** The equations for a compressible, inviscid, infinitely conducting plasma are:

$$\begin{aligned}
 \rho \frac{d\vec{v}}{dt} &= -\vec{\nabla} \cdot \vec{p} + \frac{1}{4\pi} (\vec{\nabla} \times \vec{B}) \times \vec{B}, \\
 \frac{\partial \rho}{\partial t} &= -\vec{\nabla} \cdot (\rho \vec{v}), \\
 \frac{\partial \vec{B}}{\partial t} &= \vec{\nabla} \times (\vec{v} \times \vec{B}), \\
 \vec{\nabla} \cdot \vec{B} &= 0, \\
 \vec{p} &= p_{\perp} \vec{I} + (p_{\parallel} - p_{\perp}) \hat{n} \hat{n}, \\
 \vec{I} &= \text{unit dyadic},
 \end{aligned}
 \tag{1}$$

and the adiabatic equations of state with generalized polytrope exponents  $\alpha, \beta, \varepsilon$ , and  $\gamma$  are [29]:

$$\frac{d}{dt} \left( \frac{p_{\parallel} B^{\alpha}}{\rho^{\gamma}} \right) = 0$$

and

$$\frac{d}{dt} \left( \frac{p_{\perp}}{\rho^{\varepsilon} B^{\beta}} \right) = 0.$$

Here,  $\parallel$  and  $\perp$  denote components parallel and perpendicular to the magnetic field respectively. For the special choices (a)  $\alpha = 0, \beta = 0, \varepsilon = \frac{5}{3}, \gamma = \frac{5}{3}$ , and (b)  $\alpha = 2, \beta = 1, \varepsilon = 1, \gamma = 3$ , this model reduces to the MHD and CGL models respectively. The equilibrium we consider (Fig. 1) has a flow velocity  $v_0(x) = v_{0y}(x)\hat{y} + v_{0z}(x)\hat{z}$ , a uniform magnetic field  $\mathbf{B} = B_0\hat{z}$ , and constant density  $\rho$ , and pressures  $p_{\parallel}$  and  $p_{\perp}$ . In Sec. III we specialize the velocity to the form  $\mathbf{v} = \pm(v_{ym}\hat{y} + v_{zm}\hat{z})$  for  $x \neq 0$ . Here  $\theta_1 = \tan^{-1}(v_{0y}/v_{0z})$  is the angle made by the flow velocity with the magnetic field, and  $\theta_2 = \tan^{-1}(k_y/k_z)$  is the angle of propagation of the mode with respect to the magnetic field.

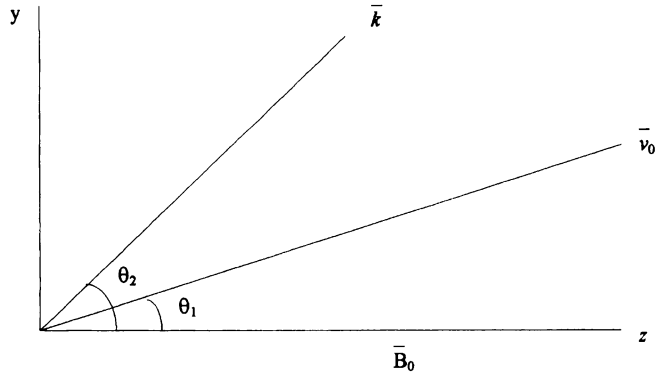


FIG. 1. Geometry of the equilibrium configuration and flow for the compressible, anisotropic linear velocity profile shear layer. The wave vector  $k$  for the perturbation quantities is shown.

The first-order perturbation quantities are of the form  $f(x) \exp[i(k_y y + k_z z - \omega t)]$ . The frequency  $\omega$  is assumed to have at least a small positive imaginary part, so that the solutions correspond to those of an initial-value problem. Linearizing Eqs. (1), we obtain

$$i\Omega\delta\rho = -\rho(\delta v'_x + ik_y\delta v_y + ik_z\delta v_z), \tag{2a}$$

$$i\Omega\rho\delta v_z + ik_z\delta p_{\parallel} + (p_{\perp} - p_{\parallel})ik_z \frac{\delta B_z}{B_0} = 0, \tag{2b}$$

$$i\Omega\rho\delta v_x + \delta p'_{\perp} + \frac{B_0}{4\pi} \delta B'_z - \frac{ik_z B_0}{4\pi} \delta B_x \left( \frac{p_{\perp} - p_{\parallel}}{B_0^2/(4\pi)} + 1 \right) = 0, \tag{2c}$$

$$i\Omega\rho\delta v_y + ik_y\delta p_{\perp} + \frac{ik_y B_0}{4\pi} \delta B_z - \frac{ik_z B_0}{4\pi} \delta B_y \left( \frac{p_{\perp} - p_{\parallel}}{B_0^2/(4\pi)} + 1 \right) = 0, \tag{2d}$$

$$\frac{\delta p_{\perp}}{p_{\perp}} = \epsilon \frac{\delta\rho}{\rho} + \beta \frac{\delta B_z}{B_0}, \tag{2e}$$

$$\frac{\delta p_{\parallel}}{p_{\parallel}} = \gamma \frac{\delta\rho}{\rho} - \alpha \frac{\delta B_z}{B_0}, \tag{2f}$$

$$i\Omega\delta B_x = ik_z B_0 \delta v_x, \tag{2g}$$

$$i\Omega\delta B_y = ik_z B_0 \delta v_y + S v'_0 \delta B_x, \tag{2h}$$

$$i\Omega\delta B_z = ik_z B_0 \delta v_z + C v'_0 \delta B_x - B_0[\delta v'_x + ik_y\delta v_y + ik_z\delta v_z], \tag{2i}$$

$$\delta B'_x + ik_y\delta B_y + ik_z\delta B_z = 0. \tag{2j}$$

Here the prime denotes a derivative with respect to  $x$ ,  $C \equiv \cos(\theta_1)$ ,  $S \equiv \sin(\theta_1)$ , and  $\Omega \equiv (k_y v_0 S + k_z v_0 C - \omega)$ . The equilibrium quantities are  $p_{\parallel}$ ,  $p_{\perp}$ ,  $\rho$ , and  $v_0(x)$ .

Now, what we wish to do is to take these linearized equations and “boil” them together into one equation that is dependent upon one variable only. Since we want to ensure that none of the physical properties is lost, we shall make use of all the equations in the process.

Equation (2f) is solved for  $\delta p_{\parallel}$ , which is then substituted into the equation obtained by eliminating  $\delta v_z$  from (2b) and (2i). This yields

$$(\vec{\nabla} \cdot \delta \vec{v}) = \chi_2 \delta B_x + \chi_3 \delta B_z, \tag{3a}$$

where

$$\chi_1 = ik_z^2 \{ (1 + \alpha) p_{\parallel} - p_{\perp} \} - i\rho\Omega^2,$$

$$\chi_2 = \rho\Omega C Q v'_0,$$

$$\chi_3 = Q\chi_1,$$

$$Q = \left[ \rho\Omega B_0 - \frac{\gamma k_z^2 B_0 p_{\parallel}}{\Omega} \right]^{-1}.$$

Next, eliminate  $\delta\rho$  from (2a) and (2e). Substituting the result and (3a) into the equation obtained by eliminating  $\delta v_y$  from (2d) and (2h) gives

$$\delta B_y = \chi_4 \delta B_x + \chi_5 \delta B_z \tag{3b}$$

where

$$\chi_6 = ik_z^2 \left( p_{\perp} - p_{\parallel} + \frac{B_0^2}{4\pi} \right) - i\rho\Omega^2,$$

$$\chi_5 = \frac{[-\frac{\epsilon k_y k_z B_0 p_{\perp} \chi_3}{\Omega} + \frac{ik_y k_z B_0^2}{4\pi} + ik_y k_z p_{\perp} \beta]}{\chi_6} \text{ or}$$

$$\chi_5 \chi_6 = -\frac{\epsilon k_y k_z B_0 p_{\perp} \chi_3}{\Omega} + \frac{ik_y k_z B_0^2}{4\pi} + ik_y k_z p_{\perp} \beta,$$

$$\chi_4 = \frac{[-\frac{\epsilon k_y k_z B_0 p_{\perp} \chi_2}{\Omega} - \rho\Omega S v'_0]}{\chi_6} \text{ or}$$

$$\chi_4 \chi_6 = -\frac{\epsilon k_y k_z B_0 p_{\perp} \chi_2}{\Omega} - \rho\Omega S v'_0.$$

Using (3b) in (2j) yields

$$\delta B_z = -\chi_7 (\delta B'_x + ik_y \chi_4 \delta B_x) \tag{3c}$$

where

$$\chi_7 = (ik_y \chi_5 + ik_z)^{-1}.$$

Using (3c) and (2g) in (2c) yields an equation for the  $x$ -component of the magnetic field perturbation:

$$\begin{aligned} \frac{i\rho\Omega^2 \delta B_x}{k_z B_0} + p_{\perp} \left[ \frac{i\epsilon(\chi_2 \delta B_x + \chi_3 \delta B_z)}{\Omega} + \beta \frac{\delta B_z}{B_0} \right]' - \frac{B_0}{4\pi} [\chi_7 (\delta B'_x + ik_y \chi_4 \delta B_x)]' \\ - \frac{ik_z B_0}{4\pi} \left( \frac{p_{\perp} - p_{\parallel}}{B_0^2/(4\pi)} + 1 \right) \delta B_x = 0, \end{aligned} \tag{4}$$

where  $\delta B_z$  is given by (3c).

Notice that we have used all the perturbation equations (2) in deriving Eq. (4). Also notice that all the physical quantities characterizing the perturbation ( $\delta v, \delta \mathbf{B}, \delta\rho, \delta p_{\parallel}, \delta p_{\perp}$ ) may be obtained in terms of  $\delta B_x$  evaluated from Eq. (4). Also, notice that for the

polytropic indices  $\alpha = 2$ ,  $\beta = \varepsilon = 1$ , and  $\gamma = 3$  corresponding to the CGL model, Eq. (4) reduces to Eq. (4) of [30].

**3. External solutions.** Outside the region of velocity shear,  $v_0 = \text{constant}$ . In the absence of velocity shear,  $\frac{d^2}{dx^2} = -k_x^2 \equiv -k_{\pm}^2$  and we recover the dispersion relation for Alfvén wave propagation in static, infinite, homogeneous, anisotropic plasma. For  $\alpha = 2$ ,  $\beta = 1$ ,  $\varepsilon = 1$ , and  $\gamma = 3$  corresponding to the CGL double adiabatic case, this leads to firehose and mirror instabilities, with these modes being coupled when velocity shear is included [20].

If we now look at the external regions, that is, where  $v'_0 = 0$  or  $v_0 = \text{constant}$ , we can solve for  $\delta B_x = \text{constant} \exp\{\pm i k_{\pm} x\}$  analytically in the external regions outside of the shear layer with the following wavenumbers:

$$k_{\pm}^2 = \frac{k_z^2 [(u_{D\pm}^2 - \gamma r^2) \{u_{D\pm}^2 - (1 - r^2 + q_D^2)\} - T^2 \{(\beta + q_D^2)(u_{D\pm}^2 - \gamma r^2) - \varepsilon((1 + \alpha)r^2 - 1 - u_{D\pm}^2)\}]}{(\beta + \varepsilon + q_D^2)(u_{D\pm}^2 - \gamma r^2) + \varepsilon\{(\gamma - 1 - \alpha)r^2 + 1\}} \quad (5)$$

where  $T = \tan \theta_2 \equiv (k_y/k_z)$ ,  $\theta_2$  is the angle of propagation of the mode to the magnetic field, and the  $\pm$  subscripts denote the two sides external to the region of velocity shear. Perturbations  $\pm\theta_2$  are equivalent and only positive  $\theta_2$  are considered. For the values  $\varepsilon = \beta = 1$ ,  $\alpha = 2$ , and  $\gamma = 3$ , Eq. (5) reduces to exactly that of the CGL case [30]. Here, we introduce the dimensionless frequency

$$W \equiv \frac{\omega}{k_z S_{\perp}} = W_r + iW_i, \quad (6a)$$

and the dimensionless flow speed

$$u_D = \frac{\Omega}{k_z S_{\perp}}, \quad (6b)$$

where  $S_{\parallel, \perp} \equiv (\frac{\rho_{\parallel, \perp}}{\rho})^{1/2}$  are the sound speeds parallel and perpendicular to the magnetic field. We also define the dimensionless anisotropy parameter

$$r = \frac{S_{\parallel}}{S_{\perp}}, \quad (6c)$$

and the ratio of the magnetic field-energy density to the perpendicular thermal-energy density (the square root of the inverse plasma beta)

$$q_D^2 \equiv \left(\frac{v_A}{S_{\perp}}\right)^2, \quad (6d)$$

where the Alfvén speed is

$$v_A^2 \equiv \frac{B_0^2}{4\pi\rho}. \quad (6e)$$

For a shear layer of width  $L$  and with a linear velocity profile,

$$\begin{aligned} v_0 &\equiv v_m (S\hat{y} + C\hat{z}) \left(\frac{x}{L}\right), & -\frac{1}{2} \leq x \leq \frac{1}{2}, \\ \Omega &\equiv (TMS + MC) \left(\frac{x}{L}\right) - W, \end{aligned} \quad (7)$$

where the Mach number of the layer is

$$M \equiv \frac{2v_m}{S_{\perp}}. \tag{8}$$

We now transform to a frame of reference co-moving with the fluid. Let us first look at the external region to the left of the shear layer, i.e.,  $x < -\frac{1}{2}$ , and look at an arbitrary point  $z$ . At time  $t$  in the “lab frame”,  $z = z$ . However, in the fluid frame,  $z' = z + v_{zm}t$ . The full dependence is

$$\delta B_x = \text{const} \exp[i(\pm k_x x + k_z z - \omega t)] = \text{const} e^{\pm i(k_{r-} + ik_{i-})x} e^{-i(\omega_r + i\omega_i)t} e^{ik_z(z' - v_{zm}t)}.$$

We can see that  $\omega = \omega_r + i\omega_i$ , in general, with  $\omega_i > 0$  for unstable wave solutions. The correct choice of the  $\pm$  signs in the external regions is determined by dual considerations. The  $x$ -component of the magnetic field perturbation  $\delta B_x$  should correspond to a spatially damping (in  $x$ ), and outgoing mode at  $x \rightarrow \pm\infty$  in the co-moving frame of the plasma in each of the external regions. If we look at the upper sign, we see that in order to have spatial damping,  $k_{i-} < 0$  and for the outgoing mode,  $k_{r-} < 0$ . If we look at the lower sign, to achieve spatial damping,  $k_{i-} > 0$  and for the outgoing mode here,  $k_{r-} > 0$ . If we examine  $k_-$  as  $W_i \rightarrow 0^+$ , making use of the binomial theorem, we can observe that the admissible signs are  $k_{r-} > 0$  and  $k_{i-} > 0$ , thus implying that the correct choice is the lower sign.

In a similar manner we can look at the external region to the right of the shear layer, i.e.,  $x > \frac{1}{2}$ , where  $z' = z - v_{zm}t$  and the full dependence is

$$\begin{aligned} \delta B_x &= \text{const} \exp[i(\pm k_+ x + k_z z - \omega t)] = \text{const} e^{\pm i(k_{r+} + ik_{i+})x} e^{-i(\omega_r + i\omega_i)t} e^{ik_z(z' + v_{zm}t)} \\ &= \text{const} \exp\{i[\pm k_+ x - \omega t + k_z(z' + v_{zm}t)]\} \exp\{\mp k_{i+} x + \omega_i t\}. \end{aligned} \tag{9b}$$

If we look at the upper sign, we see that in order to have spatial damping,  $k_{i+} > 0$  and for the outgoing mode,  $k_{r+} < 0$ . If we look at the lower sign, to achieve spatial damping,  $k_{i+} < 0$  and for the outgoing mode here,  $k_{r+} > 0$ . If we examine  $k_+$  as  $W_i \rightarrow 0^+$ , making use of the binomial theorem, we can observe that the admissible signs are  $k_{r+} > 0$  and  $k_{i+} < 0$ , thus implying that the correct choice is the lower sign. Since both external regions agree on the lower sign, that is the one that we will consider with  $k_{r-} > 0$  and  $k_{i-} > 0$  to the left of the shear layer (the B.C.’s) and  $k_{r+} > 0$  and  $k_{i+} < 0$  to the right of the shear layer.

The conditions above on the real and imaginary parts of  $k_{\pm}$  may be combined yielding:

$$\text{a) } \text{Im } k_-^2 = 2k_{r-}k_{i-} > 0, \tag{10a}$$

$$\text{b) } \text{Im } k_+^2 = 2k_{r+}k_{i+} < 0, \tag{10b}$$

Using (5) and (6), one may write these conditions for the existence of spatially damping, outgoing waves as

$$(\phi_{2-} - T^2\phi_{4-})\phi_{5-} - (\phi_{1-} - T^2\phi_{3-})\phi_{6-} > 0 \tag{11a}$$

and

$$(\phi_{2+} - T^2\phi_{4+})\phi_{5+} - (\phi_{1+} - T^2\phi_{3+})\phi_{6+} < 0. \tag{11b}$$

Here,

$$\begin{aligned} m_{1\pm} &\equiv \left[ \frac{\pm(\text{TMS} + \text{MC})}{2} - W_r \right]^2 - W_i^2, \\ m_{2\pm} &\equiv 2W_i \left[ \frac{\pm(\text{TMS} + \text{MC})}{2} - W_r \right], \\ \phi_{1\pm} + i\phi_{2\pm} &\equiv (m_{1\pm} - im_{2\pm} - \gamma r^2)(m_{1\pm} - im_{2\pm} - 1 + r^2 - q_D^2), \\ \phi_{3\pm} + i\phi_{4\pm} &\equiv (\beta + q_D^2)(m_{1\pm} - im_{2\pm} - \gamma r^2) - \varepsilon[(1 + \alpha)r^2 - 1 - m_{1\pm} + im_{2\pm}], \\ \phi_{5\pm} + i\phi_{6\pm} &\equiv (\beta + \varepsilon + q_D^2)(m_{1\pm} - im_{2\pm} - \gamma r^2) - \varepsilon[(\gamma - 1 - \alpha)r^2 + 1]. \end{aligned}$$

**4. Zero-width layer.** Velocity shear layers of zero width, i.e.,

$$v_0(x) = \begin{cases} v_m(S\hat{y} + C\hat{z}), & x > 0, \\ -v_m(S\hat{y} + C\hat{z}), & x < 0 \end{cases} \quad (12)$$

are also referred to as “tangential velocity discontinuities” or, for the fluid dynamical case, as “vortex sheets” [10], [27], [30]. The conventional approach in this case is to start with the equations (2) for perturbed field variables and match quantities on the two sides of the discontinuity at  $x = 0$  so as to satisfy the boundary conditions [10]: i) the normal velocity is continuous; ii) the normal magnetic field is continuous; and iii) the normal total, Reynolds’ (fluid) plus Maxwell (electromagnetic) stress, is continuous across the interface. However, the dispersion relation obtained in this manner is more easily derived by integrating the composite equation (4) across the discontinuity. In doing this, it is necessary to remember that all quantities are continuous across the jump, with the exception of  $v_0$ , so that  $(\frac{dv_0}{dx})$  contains a Kronecker delta. This procedure automatically takes into account the boundary conditions mentioned above, as may be explicitly verified, since all the perturbation equations (2) are incorporated in (4).

Integrating (4) across the jump at  $x = 0$ , and denoting quantities for  $x > 0$  and  $x < 0$  respectively by subscripts  $+$  and  $-$  as before, we obtain

$$\chi_{7+} k_+ \left[ p_{\perp} \left( \frac{i\varepsilon\chi_3}{\Omega} + \frac{\beta}{B_0} \right) + \frac{B_0}{4\pi} \right]_+ = \chi_{7-} k_- \left[ p_{\perp} \left( \frac{i\varepsilon\chi_3}{\Omega} + \frac{\beta}{B_0} \right) + \frac{B_0}{4\pi} \right]_-, \quad (13)$$

where we have used the fact that  $\delta B_x = \text{constant} \exp\{-ik_{\pm}x\}$  on the two sides of the discontinuity.

Using (5) and the definitions of  $\chi_3$  and  $\chi_7$ , (13) yields the dispersion relation

$$\begin{aligned} \left(\frac{\omega}{k}\right)^4 - 2\left(\frac{\omega}{k}\right)^2 (v_m^2 + \gamma S_{\parallel}^2) + \left[ v_m^4 - 2\gamma S_{\parallel}^2 \left(\frac{\omega}{k}\right)^2 + \gamma^2 S_{\parallel}^4 \right] \\ - \frac{\varepsilon S_{\perp}^2 (\gamma S_{\parallel}^2 + S_{\parallel}^2 - S_{\perp}^2 - v_A^2) [S_{\perp}^2 + (\gamma - \alpha - 1) S_{\parallel}^2]}{v_A^2 + (\varepsilon + \beta) S_{\perp}^2} = 0. \end{aligned} \quad (14)$$

Here,  $k \equiv (k_y^2 + k_z^2)^{1/2}$ . On substituting the double adiabatic values  $\alpha = 2$ ,  $\beta = \varepsilon = 1$ ,  $\gamma = 3$  for the polytrope indices, (14) reduces to the dispersion relation obtained earlier by Talwar [27] for the CGL case. Note that (13) was squared in obtaining (14), so that the dispersion relation (14) contains spurious solutions in addition to genuine ones. The solutions are thus to be “tested out” by substituting back into (13). More easily,

the spurious solutions of (14) may be identified and discarded since their growth rates ( $\omega_i = (k_z S_\perp) W_i$ ) do not vanish when the velocity discontinuity  $v_m$  driving the instability goes to zero.

The stability of the zero-width layer depends upon the nature of the roots of (14). If all roots for  $(\frac{\omega}{k})$  of (14) are real, the configuration is linearly stable. By contrast, if a)  $(\frac{\omega}{k})^2$  is real negative, one has monotonic instability [10] with  $\omega_r = 0$ , while for b)  $(\frac{\omega}{k})^2$  complex, the shear layer exhibits oscillatory instability or overstability [10] with  $\omega_r \neq 0$ . The conditions for each of the three possibilities are thus

$$v_A^2 + (\varepsilon + \beta) S_\perp^2 > \frac{\varepsilon S_\perp^2 [S_\perp^2 + (\gamma - \alpha - 1) S_\parallel^2] [(\gamma + 1) S_\parallel^2 - S_\perp^2 + (\varepsilon + \beta) S_\perp^2]}{(U^2 - \gamma S_\parallel^2)^2 + \varepsilon [S_\perp^2 + (\gamma - \alpha - 1) S_\parallel^2] S_\perp^2} \quad (15a)$$

for stability,

$$v_A^2 + (\varepsilon + \beta) S_\perp^2 < \frac{\varepsilon S_\perp^2 [S_\perp^2 + (\gamma - \alpha - 1) S_\parallel^2] [(\gamma + 1) S_\parallel^2 - S_\perp^2 + (\varepsilon + \beta) S_\perp^2]}{(U^2 - \gamma S_\parallel^2)^2 + \varepsilon [S_\perp^2 + (\gamma - \alpha - 1) S_\parallel^2] S_\perp^2} \quad (15b)$$

for monotonic instability, and

$$v_A^2 + (\varepsilon + \beta) S_\perp^2 > \frac{\varepsilon S_\perp^2 [S_\perp^2 + (\gamma - \alpha - 1) S_\parallel^2] [(\gamma + 1) S_\parallel^2 - S_\perp^2 + (\varepsilon + \beta) S_\perp^2]}{\varepsilon S_\perp^2 [S_\perp^2 + (\gamma - \alpha - 1) S_\parallel^2] - 4\gamma S_\parallel^2 v_m^2} \quad (15c)$$

for oscillatory instability. The numerators in (15a–c) are the same, but the denominators of (15a–b) are larger than that of (15c). Hence, the zero-width layer is stable for small values of  $v_A^2 + (\varepsilon + \beta) S_\perp^2$ , monotonically unstable for values of  $v_A^2 + (\varepsilon + \beta) S_\perp^2$  intermediate between the right-hand sides of (15b) and (15c), and exhibits oscillatory (overstable) instability for large values of  $v_A^2 + (\varepsilon + \beta) S_\perp^2$ .

The earlier conditions for stability/instability of a) collisionless anisotropic (CGL) shear layers [27] with  $\alpha = 2$ ,  $\beta = \varepsilon = 1$ ,  $\gamma = 3$ , and b) collision-dominated isotropic (MHD) plasma [12–14] with  $\alpha = \beta = 0$ ,  $\varepsilon = \gamma = \frac{5}{3}$ ,  $S_\perp^2 = S_\parallel^2 = S^2$  may all be recovered from (15) with the appropriate values for the polytrope indices.

**5. Numerical technique for finite-width layers.** Next, we shall consider the instability of a shear layer of width  $L$  and having a linear velocity profile given by (7). The numerical solution of the perturbation equations makes use of the fact that in the regions external to the region of linear velocity shear,  $|\frac{x}{L}| > \frac{1}{2}$  (see (7)), analytic solutions of the pressure (or velocity) perturbation equations are known. The constraint of outgoing and spatially damping waves in both regions enables us to pick the appropriate solution in each region (see (9) and (10)).

Before we solve numerically, it will be to our benefit to nondimensionalize Eq. (4). To do so we will divide through by  $(k_z S_\perp^2) \rho$ . Some new quantities will be defined in the

process:

$$\bar{x} = \frac{x}{L} \text{ where } L \text{ is the width of the shear layer,} \tag{16a}$$

$$\frac{\delta B_x}{B_0} \equiv \delta b_x, \tag{16b}$$

$$\frac{\delta B_y}{B_0} \equiv \delta b_y, \tag{16c}$$

$$\frac{\delta B_z}{B_0} \equiv \delta b_z, \tag{16d}$$

$$u_D \equiv \frac{\Omega}{k_z S_\perp} = \bar{x}(TMS + MC) - W, \quad W \equiv \frac{\omega}{k_z S_\perp}, \tag{16e}$$

$$K_z = k_z L. \tag{16f}$$

When the process is complete, the final nondimensional equation is

$$\begin{aligned} & iu_D^2 \delta b_x + \frac{1}{K_z^2} \left[ \frac{i\epsilon CM \delta b_x}{\left(u_D - \frac{\gamma r^2}{u_D}\right)} - \left\{ \frac{\epsilon u_D^2 - (1 + \alpha)r^2 \epsilon + \epsilon}{(u_D^2 - \gamma r^2)} + \beta \right\} \right. \\ & \times \left. \left\{ \frac{(1 - r^2 + q_D^2 - u_D^2)}{[\Gamma^2(-\epsilon \Gamma_1 + i\beta + iq_D^2) + i(1 - r^2 + q_D^2 - u_D^2)]} \right\} (\delta b'_x + iK_y \chi_4 \delta b_x) \right]' \\ & - \frac{q_D^2}{K_z^2} \left[ \left\{ \frac{(1 - r^2 + q_D^2 - u_D^2)}{[\Gamma^2(-\epsilon \Gamma_1 + i\beta + iq_D^2) + i(1 - r^2 + q_D^2 - u_D^2)]} \right\} \right] \\ & \times \left( \delta b'_x - T \left[ \frac{\epsilon T \left( \frac{CM}{\left(u_D - \frac{\gamma r^2}{u_D}\right)} \right) + SMu_D}{1 - r^2 + q_D^2 - u_D^2} \right] \delta b_x \right)' - i(1 - r^2 + q_D^2) \delta b_x = 0, \end{aligned} \tag{17}$$

where

$$(\delta b'_x + iK_y \chi_4 \delta b_x) = \left( \delta b'_x - T \left[ \frac{\epsilon T \left( \frac{CM}{\left(u_D - \frac{\gamma r^2}{u_D}\right)} \right) + SMu_D}{1 - r^2 + q_D^2 - u_D^2} \right] \delta b_x \right),$$

$$T \equiv \tan \theta_2 = \frac{k_y}{k_z},$$

$$\Gamma_1 = \frac{i\{(1 + \alpha)r^2 - 1\} - iu_D^2}{u_D^2 - \gamma r^2},$$

and  $' \equiv \frac{d}{d\bar{x}}$ .

To solve this numerically we need to separate the real and imaginary parts. There are two quantities in the equation that are complex:  $u_D = u_{Dr} + iu_{Di} = (TMS + MC)\bar{x} - (W_r + iW_i)$ ;  $b_x = b_{xr} + ib_{xi}$ . This task is quite cumbersome and requires a lot of algebra. When we are finished we have a set of two coupled second-order differential equations. The strategy employed in the numerical integration of these equations is as follows: For a given point in the  $K_z/M$  plane, we choose a value of  $\omega = \omega_r + i\omega_i$ . We then select the correct outgoing, damping solution for the region  $\bar{x} < -\frac{1}{2}$ , which is used to set

the boundary conditions on  $\delta b_{xr}$ ,  $\delta b_{xi}$ ,  $\delta b'_{xr}$ , and  $\delta b'_{xi}$  at  $\bar{x} = -\frac{1}{2}$ . The coupled set of differential equations is then integrated across the shear layer to  $\bar{x} = \frac{1}{2}$ . The solution at  $\bar{x} = \frac{1}{2} - 0$  is then matched to the analytic solution in the external region  $\bar{x} \geq \frac{1}{2}$ . In general, that is, for the “wrong” choice of  $\omega$ , the numerical solution for  $\bar{x} > \frac{1}{2}$  consists of an outgoing damping component as well as an incoming growing one. However, for the correct values of  $\omega$ , only an outgoing damping component occurs. A “shooting” technique is used to locate the “correct” values of  $\omega$ .

For  $\bar{x} < -\frac{1}{2}$ , the equation for the pressure perturbation has the solutions

$$\delta b_x = \text{const exp}\{\pm ik_- \bar{x}\}$$

where

$$k_- = k_{r-} + ik_{i-} = B[(A + W_r + iW_i)^2 - 1]^{1/2}.$$

As discussed, the correct boundary conditions of spatially damping, outgoing solutions imply that  $\delta b_x = \text{constant exp}\{-ik_- \bar{x}\}$  for  $\bar{x} \leq -\frac{1}{2}$ . Hence, “boundary” conditions at  $\bar{x} = -\frac{1}{2}$  (or  $\bar{x} < -\frac{1}{2}$ ) are

$$\delta b_x = \text{exp}\{k_{i-} \bar{x}\} [\cos(k_{r-} \bar{x}) - i \sin(k_{r-} \bar{x})] \tag{18a}$$

and

$$\begin{aligned} \delta b'_x &= [k_{i-} \cos(k_{r-} \bar{x}) - k_{r-} \sin(k_{r-} \bar{x})] \text{exp}\{k_{i-} \bar{x}\} \\ &\quad - i[k_{i-} \sin(k_{r-} \bar{x}) + k_{r-} \cos(k_{r-} \bar{x})] \text{exp}\{k_{i-} \bar{x}\}. \end{aligned} \tag{18b}$$

The factor  $\text{exp}\{k_{i-} \bar{x}\}$  in the above equations may be set to unity since it only affects the amplitudes of the boundary conditions and hence the resulting solutions. The values of  $\delta b_x$  and  $\delta b'_x$  at  $\bar{x} = -\frac{1}{2}$  are used in the  $\bar{x}$ -integration of the equation for the pressure perturbation. In that the perturbation equations are linearized, the amplitude of  $\delta b_x$  at, say,  $\bar{x} = -\frac{1}{2}$  may be chosen arbitrarily.

We now discuss the technique of ensuring that we match onto the desired damping and outgoing solutions at  $\bar{x} = \frac{1}{2}$ . The numerical integration through the shear layer gives us  $\delta b_x$  and  $\delta b'_x$  at  $\bar{x} = +\frac{1}{2}$ . For  $\bar{x} > \frac{1}{2}$ , the solutions are  $\delta b_x = \text{const exp}\{\pm ik_+ \bar{x}\}$  where  $k_+ = k_{r+} + ik_{i+} = B[(A - W_r - iW_i)^2 - 1]^{1/2}$ . From considerations analogous to those used in the region  $\bar{x} < -\frac{1}{2}$ , we find that for spatially damped, outgoing waves we need  $\delta b_x = \text{const exp}\{-ik_+ \bar{x}\}$  for  $(A - W_r) > 0$  and  $\delta b_x = \text{const exp}\{ik_+ \bar{x}\}$  for  $(A - W_r) < 0$ . As mentioned earlier, we assume  $W_r > 0$ .

Evidently, the general solutions for  $\bar{x} > \frac{1}{2}$  may be written as

$$\delta b_x = c_1 \text{exp}[+ik_+ (\bar{x} - \frac{1}{2})] + c_2 \text{exp}[-ik_+ (\bar{x} - \frac{1}{2})], \tag{19}$$

where  $c_1 = c_{1r} + ic_{1i}$  and  $c_2 = c_{2r} + ic_{2i}$  are complex quantities. Solving this equation for the constants at  $\bar{x} = \frac{1}{2}$  gives

$$c_{1r} = \left[ \frac{1}{2} \delta b_{xr} - \frac{(k_{i+} \delta b'_{xr} - k_{r+} \delta b'_{xi})}{2(k_{i+}^2 + k_{r+}^2)} \right]_{\frac{1}{2}}, \quad (20a)$$

$$c_{2r} = \left[ \frac{1}{2} \delta b_{xr} + \frac{(k_{i+} \delta b'_{xr} - k_{r+} \delta b'_{xi})}{2(k_{i+}^2 + k_{r+}^2)} \right]_{\frac{1}{2}}, \quad (20b)$$

$$c_{1i} = \left[ \frac{1}{2} \delta b_{xi} - \frac{(k_{i+} \delta b'_{xi} + k_{r+} \delta b'_{xr})}{2(k_{i+}^2 + k_{r+}^2)} \right]_{\frac{1}{2}}, \quad (20c)$$

$$c_{2i} = \left[ \frac{1}{2} \delta b_{xi} + \frac{(k_{i+} \delta b'_{xi} + k_{r+} \delta b'_{xr})}{2(k_{i+}^2 + k_{r+}^2)} \right]_{\frac{1}{2}}, \quad (20d)$$

where the subscript  $\frac{1}{2}$  denotes quantities evaluated at  $\bar{x} = \frac{1}{2}$ .

For specificity, assume that  $(A - W_r) > 0$  so that the spatially damped outgoing term of Eq. (11) has the coefficient  $c_2$ . The term with coefficient  $c_1$  is then unphysical. A useful measure of the relative magnitude of the unphysical term is

$$\text{TOL} = \frac{|\text{coefficient of } e^{ik_+\bar{x}}|^2}{|\text{coefficient of } e^{-ik_+\bar{x}}|^2} = \left( \frac{c_{1r}^2 + c_{1i}^2}{c_{2r}^2 + c_{2i}^2} \right) \exp(+2k_{i+}). \quad (21)$$

An exact physical solution of the pressure perturbation equation will have  $\text{TOL} = 0$ . On the other hand, for the integration of the pressure perturbation equation we start from  $\bar{x} = -\frac{1}{2}$  using  $\delta b_x$  and  $\delta b'_x$  from Eqs. (10) and a guess for the dimensionless frequency  $W = W_r + iW_i$ . The integration gives us the values of  $\delta b_x$  and  $\delta b'_x$  at  $\bar{x} = \frac{1}{2}$ , and, consequently, the values of  $c_{1r}$ ,  $c_{1i}$ ,  $c_{2r}$ , and  $c_{2i}$  from Eqs. (12). In turn,  $\text{TOL}$  may be evaluated from Eq. (13). In general, the choice of the frequency  $W$  will be wrong and  $\text{TOL}$  will be of order unity. The physical solutions and their corresponding  $W$  values are found by locating the valleys of  $\text{TOL}(W_r, W_i)$  in the  $(W_r, W_i)$ -plane. We consider that the existence of a physical solution is indicated, but not proven, by the values of  $\text{TOL}$  less than  $10^{-7}$  for the profile across the shear layer. This is strongly supported by the smooth and monotonic decrease of  $\text{TOL}$  in the vicinity of a valley.

The numerical integration from  $\bar{x} = -\frac{1}{2}$  to  $\bar{x} = +\frac{1}{2}$  was carried out by a standard Runge-Kutta integrator. In generating the tables in Sec. 6, approximately 200 unsuccessful integrations were performed before  $\text{TOL}$  reached the desired accuracy. In many cases,  $\text{TOL}$  actually exceeded the accuracy by several orders of 10. Both the location of a valley in the  $(W_r, W_i)$ -plane and the minimum value of  $\text{TOL}$  determined were unaffected by changes in the error criterion for the integrator.

**6. Results and conclusions.** The Kelvin-Helmholtz instability in a homogeneous, inviscid, plasma has been investigated for both zero-width and finite-width (with a "linear" velocity profile) shear layers. The instability structure in the  $(K_z, M)$ -plane is very different for the two cases.

A. *Zero-width layer (tangential velocity discontinuity)*. Equations (15) may be recast as

$$q_D^2 + (\varepsilon + \beta) < \frac{\varepsilon[(1 + (\gamma - \alpha - 1)r^2)[(\gamma + 1)r^2 - 1 + (\varepsilon + \beta)]]}{\left(\frac{M^2}{4} - \gamma r^2\right)^2 + \varepsilon[1 + (\gamma - \alpha - 1)r^2]} \quad (22a)$$

for stability,

$$q_D^2 + (\varepsilon + \beta) > \frac{\varepsilon[(1 + (\gamma - \alpha - 1)r^2)[(\gamma + 1)r^2 - 1 + (\varepsilon + \beta)]]}{\left(\frac{M^2}{4} - \gamma r^2\right)^2 + \varepsilon[1 + (\gamma - \alpha - 1)r^2]} \quad (22b)$$

for monotonic instability, and

$$q_D^2 + (\varepsilon + \beta) > \frac{\varepsilon[(1 + (\gamma - \alpha - 1)r^2)[(\gamma + 1)r^2 - 1 + (\varepsilon + \beta)]]}{\varepsilon[1 + (\gamma - \alpha - 1)r^2] - \gamma M^2 r^2} \quad (22c)$$

for oscillatory instability. Hence, for the CGL values  $\alpha = 2, \beta = \varepsilon = 1, \gamma = 3$ , (22c) implies that the supersonic speeds relevant in extragalactic jets and in the solar wind would prevent traveling wave instability in the cases  $q_D = 0.1, r = 2$  and  $q_D = 0.5, r = 2$ . However, the case with  $q_D = 0.1, r = 0.2$  would be overstable at supersonic speeds. The cases with  $r = 2$  would, however, suffer from monotonic instability even for supersonic flow speeds. For the linear velocity profile shear layer, the criteria for spatially damping and outgoing standing and traveling wave modes are very different and are given in Sec. 3. Using the inequalities (11) discussed there, we find that unstable standing wave modes exist at all values of the Mach number for the cases  $q_D = 0.1, r = 2$  and  $q_D = 0.5, r = 2$ . However, in the case with  $q_D = 0.1$  and  $r = 0.2$ , we require  $M > 1.33$  for the existence of the standing wave modes. Criteria (22) imply that unstable standing wave modes do not exist for the vertex sheet in this case.

The instability of the compressible, anisotropic vortex sheet is very different from that of the compressible, fluid dynamical vortex sheet. The fluid dynamical vortex sheet exhibits unstable standing wave modes at small Mach numbers [14]. No unstable traveling waves exist. In contrast, the anisotropic CGL vortex sheet exhibits unstable traveling modes at low values of the Mach number

$$M < M_t = \sqrt{\frac{1 + q_D^2 - 4r^2}{3r^2(2 + q_D^2)}} < \frac{1}{\sqrt{3}r}$$

if the conditions of Eq. (22c) are valid. If inequality (22c) is violated, unstable standing waves exist in a range of Mach numbers given in Eq. (22b). This behavior is similar to that exhibited by the MHD vortex sheet [12–14] where unstable traveling waves and a stable-overstable transition occur at small Mach numbers, while unstable standing wave solutions exist at larger Mach numbers.

B. *Linear velocity profile shear layer*. For the finite-width “linear” velocity profile shear layer, Tables 1–4 summarize the results of minimizing TOL at different points of the Mach number ( $M = 2v_m/S_\perp$ )/wave number ( $K_z = k_z L$ ) plane. For different values of the polytrope indices we can see that standing wave solutions having  $\omega_r = 0$  are found to exist. In addition, there are traveling wave solutions with  $\omega_r \neq 0$ . Although we consider only  $\omega_r \geq 0$ , there is for any mode with frequency  $\omega_r$  an equivalent mode with frequency  $-\omega_r$  owing to the assumed symmetry of the shear layer about  $x = 0$ .

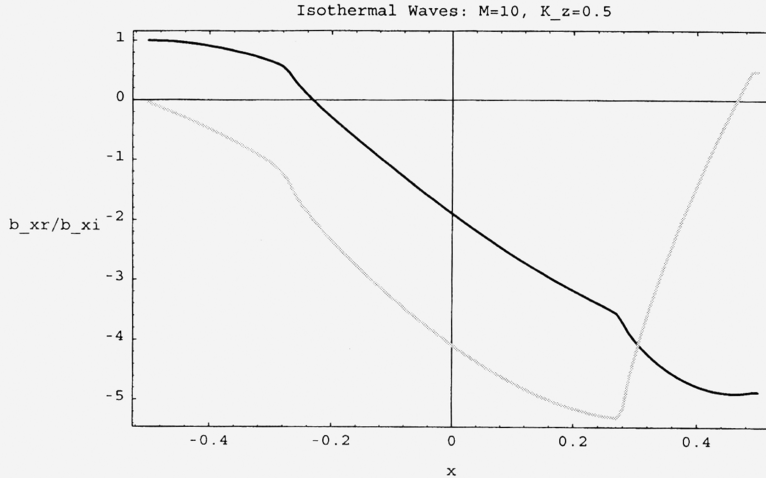


FIG. 2. Real (dark) and imaginary (light) parts of  $\delta b_x$  in the isothermal case for  $M = 10$ ,  $K_z = 0.5$ , with  $r = 4$  and  $q_D = 0.1$ . Here,  $\omega = 0.04739685 + i0.0028621$  in units of  $(S_\perp/L)$ ;  $k_- = 3.964 + i0.00302$  and  $k_+ = 3.877 - i0.00306$  in units of  $(1/L)$ . On the left-hand side of the layer,  $\delta b_x \propto \exp(-ik_- \bar{x})$ , and on the right-hand side,  $\delta b_x \propto \exp(-ik_+ \bar{x})$ .

Given the complexity of the governing equations (17) and the process of decomposing it into real and imaginary parts for the numerical solution, the code was the first benchmarked against the results for the CGL (double adiabatic) case of [20]. All the numerical results in Fig. 2 ( $q_D = 0.1, r = 4$ ) and Tables I and II ( $q_D = 0.1, r = 2$ ) of [20] are recovered for the special CGL polytropic indices  $\alpha = 2$ ,  $\beta = 1$ ,  $\varepsilon = 1$ , and  $\gamma = 3$  ( $\theta_1 = 0$  and  $\theta_2 \approx 0$ ; since  $T = \tan \theta_2$  is in the denominator of this system, it cannot be identically zero).

Unstable traveling modes occur at all values of the Mach number. The occurrence of the traveling modes is associated with the existence of a “resonant layer” where the coefficient of the second-derivative term in (9) goes through zero. We show two plots for resonant cases in Figures 2 and 3. Figure 2 corresponds to  $M = 10$ ,  $K_z = 0.5$ ,  $q_D = 0.1$ ,  $r = 4$  in the isothermal case; Figure 3 corresponds to  $M = 10$ ,  $K_z = 0.5$ ,  $q_D = 0.1$ ,  $r = 4$  in the mixed wave case. In comparing these with the corresponding plots in Figs. 4 and 9 of [20], note that [20] uses a different physical variable  $\delta V$  from the  $\delta b_x$  used here. The resonant layer is present for  $W_r < M/2$ , which is numerically found to be true in all cases. The importance of the resonant layer in giving rise to the traveling wave modes will be examined for the isothermal wave case and the mixed wave case. For an asymptotic analysis of the role of the resonant layer in driving the traveling wave instability, see [31].

If we consider the isothermal wave case, we can find its resonant layer. Let us look at the traveling wave mode seen at  $M = 10$  and  $K_z = 0.5$  with  $r = 4$  and  $q_D = 0.1$ . The resonant layer occurs where there is a kink in the profile across the layer. We can see

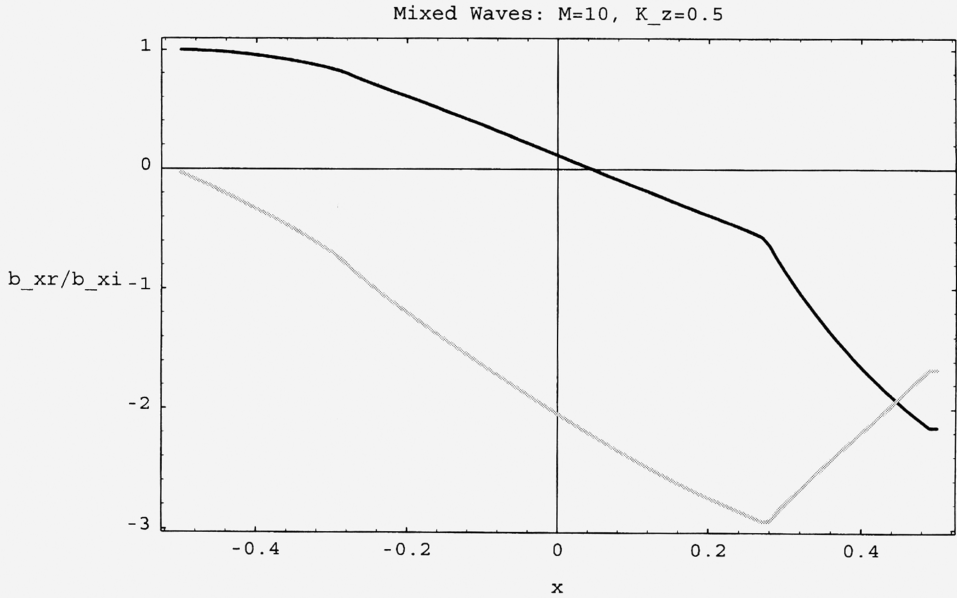


FIG. 3. Real (dark) and imaginary (light) parts of  $\delta b_x$  in the isothermal case for  $M = 10$ ,  $K_z = 0.5$ , with  $r = 4$  and  $q_D = 0.1$ . Here,  $\omega = 0.0138555 + i0.00330225$  in units of  $(S_\perp/L)$ ;  $k_- = 2.786 + i0.00264$  and  $k_+ = 2.768 - i0.00265$  in units of  $(1/L)$ . On the left-hand side of the layer,  $\delta b_x \propto \exp(-ik_- \bar{x})$ , and on the right-hand side,  $\delta b_x \propto \exp(-ik_+ \bar{x})$ .

from Fig. 2 that there are two kinks and thus two resonant layers in this case. They are symmetric about  $\bar{x}_* = 0$  at  $\bar{x}_* \approx \pm 2.7$ .

If we consider the mixed wave case, we can also identify a resonant layer. If we use the traveling wave mode at  $M = 12$  and  $K_z = 1.0$  with  $r = 4$  and  $q_D = 0.1$ , we can see in Fig. 3 that there is only one distinct kink here on the positive side of the shear layer at  $\bar{x}_* \approx +2.7$ .

Let us consider Table 1. This table corresponds to the polytrope indices for the case of isothermal waves. Along the constant Mach number slices there is a continuous increase in the growth rate, with  $\omega_i$  increasing as  $K_z$  increases. The strongest instability here is at short wavelengths, with weaker instability (lower growth rates) at longer wavelengths. Below  $M = 8$ , there is no instability due to the strong stabilization due to a fairly strong magnetic field with  $q_D = 0.1$ . At  $M = 8$  we get weak instability that increases as  $M$  is increased further. The strongest instability is observed along the slice  $M = 12$  at wavenumber  $K_z = 10$ , where  $\omega_i \approx 2.3$  in units of  $(S_\perp/L)$ . As the Mach number  $M$  increases beyond 12, the growth rates decrease again, and become confined to large wavenumbers.

Figure 4 shows the  $\delta b_{xr}$  and  $\delta b_{xi}$  profiles for an unstable mode of isothermal waves with  $M = 10$  and  $K_z = 5$  with  $q_D = 0.1$  and  $r = 4$ . The  $k_{x\pm}$  values are approximately 40 in units of  $(1/L)$ , while  $k_z$  has the value 5. Hence the magnitudes of the  $x$  and  $z$  wavenumbers are comparable.

TABLE 1. Values of  $\omega_r$  and  $\omega_i$  in units of  $(S_{\perp}/L)$  with  $q_D = 0.1$  and  $r = 4$ . The values of the polytrope indices are  $\alpha = 0$ ;  $\beta = 0$ ;  $\gamma = 1$ ;  $\varepsilon = 1$  corresponding to isothermal waves with  $\theta_1 = \theta_2 = \pi/4$ . The first number in each box corresponds to  $\omega_r$  and the second to  $\omega_i$ .

$\frac{K_z}{M}$	0.1	0.5	1.0	2.0	5.0	10.0
8	0.0000418					
	0.000228					
10	0.01473	0.04739685	0.13921	0.1444	0.368	1.666
	0.00336	0.0028621	0.043405	0.12836	0.4215	1.493
12	0.018864	0.061288	0.08264	0.32494	1.04835	0.985
	0.0057597	0.00619755	0.048202	0.15506	0.7928	2.305
15	0.01731	0.07342	0			
	0.00405	0.00541435	0.0481			

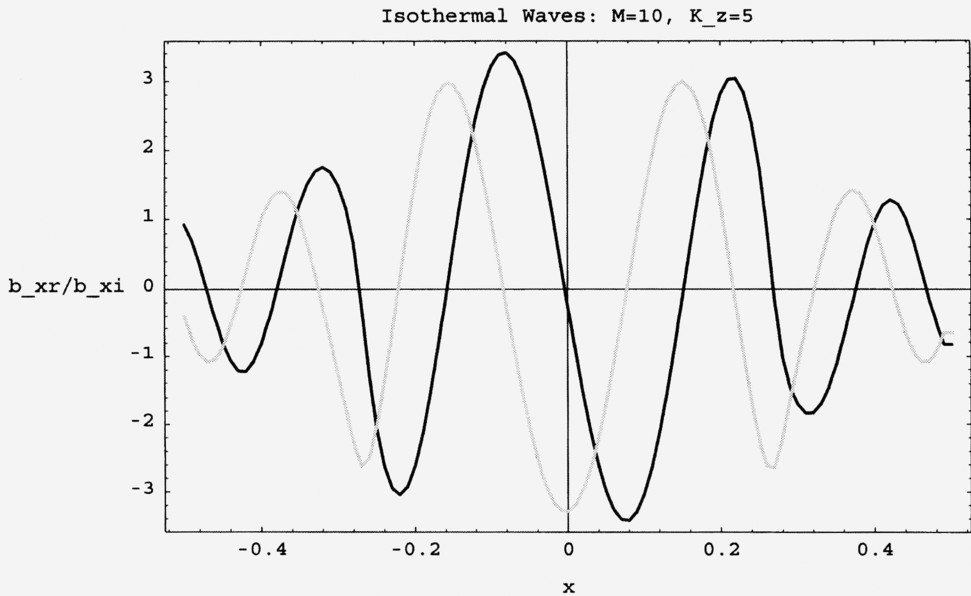


FIG. 4. Real (dark) and imaginary (light) parts of  $\delta b_x$  for the isothermal waves case with  $M = 10$  and  $K_z = 5$  and with  $q_D = 0.1$  and  $r = 4$ . For this case,  $\omega = 0.368 + i0.4215$  in units of  $(S_{\perp}/L)$ ;  $k_- = 39.544 + i0.4453$ ; and  $k_+ = 38.871 - i0.4496$  in units of  $(1/L)$ .

Now we will go to Table 2. This table corresponds to the polytrope indices for the mixed waves case. In the constant Mach number slice with  $M = 10$ , the growth increases as in Table 1. However, in the slice  $M = 12$ , we have a maximum at  $K_z = 0.1$ ; and in the slice  $M = 15$ , we have a maximum at  $K_z = 1.0$ . These slices indicate that the strongest

TABLE 2. Values of  $\omega_r$  and  $\omega_i$  in units of  $(S_{\perp}/L)$  with  $q_D = 0.1$  and  $r = 4$ . The values of the polytrope indices are  $\alpha = 0$ ;  $\beta = 1$ ;  $\gamma = 1$ ;  $\varepsilon = 1$  corresponding to mixed waves with  $\theta_1 = \theta_2 = \pi/4$ . The first number in each box corresponds to  $\omega_r$  and the second to  $\omega_i$ .

$M \backslash K_z$	0.1	0.5	1.0	2.0	5.0	10.0
8	0					
	0.0517					
10	0.0078807	0.0138555	0.0201518	0.13936	0.8125	2.561
	0.003656	0.00330225	0.0048647	0.0359	0.37995	1.273
12	0.0142	0.097812	0.1874			
	0.006153	0.0039005	0.000581			
15	0.01024	0.05219	0.10595	0.0026		
	0.005981	0.0075092	0.020878	0		

instability is at long wavelengths, with weaker growth at shorter wavelengths. Here again, as in Table 1, there is no instability below  $M = 8$  due to the strong stabilization effect of the magnetic field,  $q_D = 0.1$ . At  $M = 8$ , we get weak instability, although not as weak as in Table 1. The instability increases as  $M$  is increased and we see the strongest instability along the slice  $M = 10$  at wavenumber  $K_z = 10$ , where  $\omega_i \approx 1.3$  in units of  $(S_{\perp}/L)$ . As the Mach number  $M$  increases beyond 10, the growth rates decrease again, and become confined to large wavenumbers.

Figure 5 shows the  $\delta b_{xr}$  and  $\delta b_{xi}$  profiles for an unstable mode of mixed waves with  $M = 10$  and  $K_z = 5$  with  $q_D = 0.1$  and  $r = 4$ . If we compare this figure to Fig. 4, we can see that the profile for a mixed wave instability is a little less oscillatory than the profile for an isothermal wave instability. The  $k_{x\pm}$  values are approximately 28 in units of  $(1/L)$ , while  $k_z$  has the value 5. Hence, once again, the magnitudes of the  $x$  and  $z$  wavenumbers are comparable.

If we take a look at Table 3 we can see that it is quite stable. This is the table for the polytrope indices corresponding to the CGL case. Along the first two constant Mach number slices ( $M = 10$  and  $M = 8$ ) there are maxima at  $K_z = 0.1$ . This would indicate that the instability is almost completely confined to long wavelengths. The same table of wave number/Mach number values with  $q_D$  reduced to 0.1 (the value used in Tables 1 and 2) was extremely unstable. We also observe that the magnitude of the magnetic field strength has an effect on the structure of the instability. Increasing the magnetic field strength by changing  $q_D$  from 0.1 to 1.0 has a stabilizing effect on the system. The growth rates  $\omega_i$  decrease slightly while the angular frequencies  $\omega_r$  increase as  $q_D$  is changed from 0.1 to 1.0. The decrease in the growth rates is because of the increased field-line tension which counteracts bending of the field lines and causes stabilization. Below the Mach number  $M = 4$ , there is no instability due to the stabilization effect of a very strong magnetic field,  $q_D = 1$ . For this same reason, we can see in this table that there is weak instability for all values of the Mach number considered. The tendency

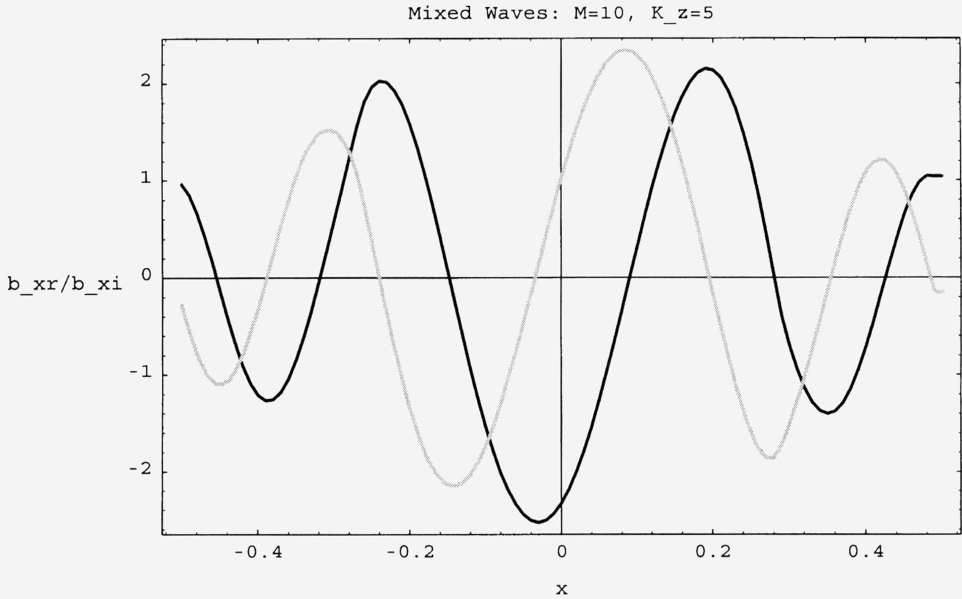


FIG. 5. Real (dark) and imaginary (light) parts of  $\delta b_x$  for the mixed waves case with  $M = 10$  and  $K_z = 5$  and with  $q_D = 0.1$  and  $r = 4$ . For this case,  $\omega = 0.8125 + i0.37995$  in units of  $(S_{\perp}/L)$ ;  $k_- = 28.2928 + i0.3005$ ; and  $k_+ = 27.2509 - i0.3095$  in units of  $(1/L)$ .

TABLE 3. Values of  $\omega_r$  and  $\omega_i$  in units of  $(S_{\perp}/L)$  with  $q_D = 1$  and  $r = 2$ . The values of the polytropic indices are  $\alpha = 2$ ;  $\beta = 1$ ;  $\gamma = 3$ ;  $\varepsilon = 1$  corresponding to the CGL case with  $\theta_1 = \theta_2 = \pi/4$ . The first number in each box corresponds to  $\omega_r$  and the second to  $\omega_i$ .

$\frac{K_z}{M}$	0.1	0.2	0.5	0.75	1.0
10	0	0.003192	0.009045	0.013473	0.017828
	0.00438	0.0022806	0.002545	0.00310125	0.003724
8	0	0.0032162	0.009305	0.0139192	0.018483
	0.0073	0.002439	0.00247	0.002709	0.003016
6	0.00023	0.002244	0.00903	0.0140482	0.01901
	0.00081	0.0022464	0.002515	0.00226725	0.00204
4	0	0	0	0	0
	0	0	0	0	0

in this table is also that the instability increases as the Mach number is increased. The strongest instability seen here is on the slice  $M = 8$  at wavenumber  $K_z = 0.1$  where  $\omega_i \approx 0.007$  in units of  $(S_{\perp}/L)$ . As was previously mentioned, the system considered by S. Roy Choudhury and Patel [20] is a special case of this general case.

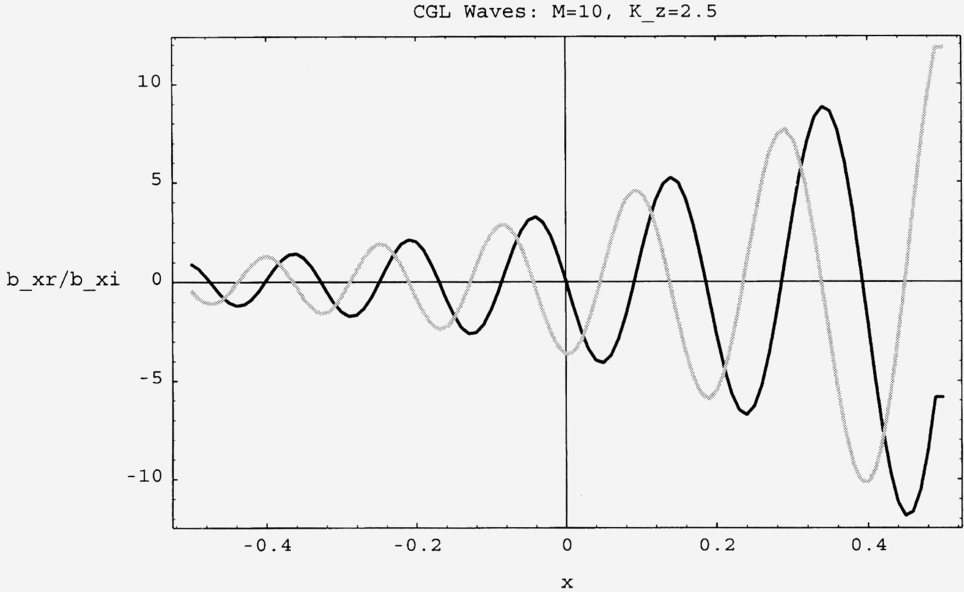


FIG. 6. Real (dark) and imaginary (light) parts of  $\delta b_x$  for the CGL case with  $M = 10$  and  $K_z = 2.5$  and with  $q_D = 0.1$  and  $r = 0.2$ . For this case,  $\omega = 8.08 + i0.5$  in units of  $(S_\perp/L)$ ;  $k_- = 44.386 + i2.214$ ; and  $k_+ = 26.720 - i2.232$  in units of  $(1/L)$ .

Figure 6 shows the  $\delta b_{xr}$  and  $\delta b_{xi}$  profiles for an unstable mode of the CGL case with  $M = 10$  and  $K_z = 2.5$  with  $q_D = 0.1$  and  $r = 0.2$  (the values corresponding to the ones in Fig. 9 of [20]). Here,  $\theta_1 = 0$  and  $\theta_2 \approx 0$ . This profile is more oscillatory than either of the previous two.

If we look at a CGL case from Table 3, we can see that the resonant layer is present. We will look at the case for  $M = 10$ ,  $K_z = 1.0$  with  $q_D = 1$  and  $r = 2$ . Figure 7 shows that there is a kink in the profile across the layer at  $\bar{x}_* \approx -0.25$ ; this time it is on the left side of the layer. The  $k_{x\pm}$  values are approximately 4 in units of  $(1/L)$ , while  $k_z$  has the value 1. Hence, once again, the magnitudes of the  $x$  and  $z$  wavenumbers are comparable.

In Table 4, the table for the polytrope indices corresponding to the MHD case, it is also quite stable. The growth rate has maxima between  $K_z = 0.75$  and  $K_z = 1.0$ . Once again, this would indicate that the instability occurs largely at long wavelengths, being stable at shorter wavelengths. This table, similar to Table 3, stabilizes mostly for  $M = 4$ , below which there is no instability due to the stabilization effect of a very strong magnetic field,  $q_D = 1$ . Again, for this same reason, we can see in this table that there is weak instability for all values of the Mach number considered. Here the strongest instability is along the slice  $M = 8$  at wavenumber  $K_z = 0.2$ , where  $\omega_i \approx 0.009$  in units of  $(S_\perp/L)$ . As the Mach number  $M$  increases beyond 8, the growth rates decrease again, and become confined to large wavenumbers.

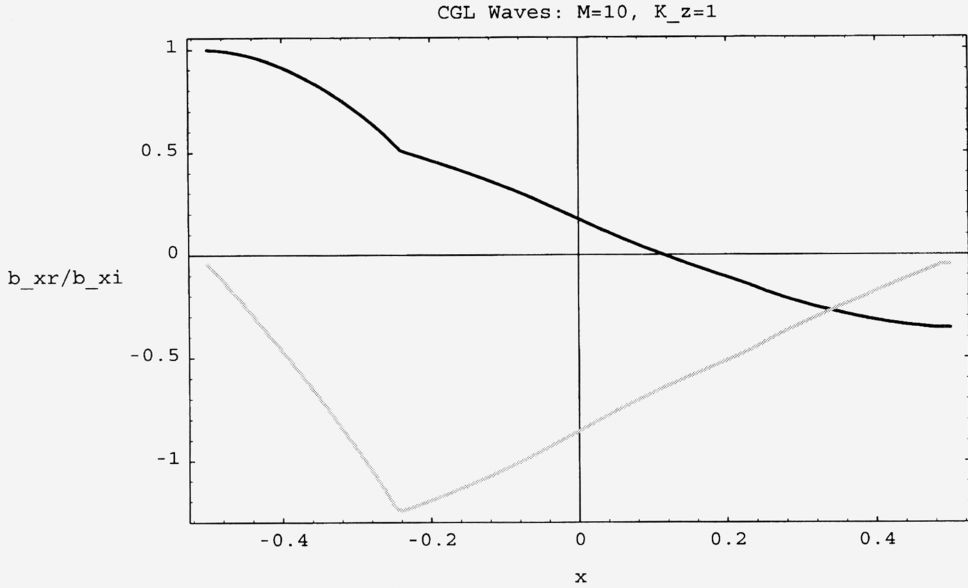


FIG. 7. Real (dark) and imaginary (light) parts of  $\delta b_x$  for the CGL case with  $M = 10$  and  $K_z = 1$  and with  $q_D = 1$  and  $r = 2$ . For this case,  $\omega = 0.017828 + i0.003724$  in units of  $(S_{\perp}/L)$ ;  $k_- = 4.032 + i0.00410$ ; and  $k_+ = 4.011 - i0.00414$  in units of  $(1/L)$ .

TABLE 4. Values of  $\omega_r$  and  $\omega_i$  in units of  $(S_{\perp}/L)$  with  $q_D = 1$  and  $r = 2$ . The values of the polytrope indices are  $\alpha = 0$ ;  $\beta = 0$ ;  $\gamma = 5/3$ ;  $\varepsilon = 5/3$  corresponding to the MHD case with  $\theta_1 = \theta_2 = \pi/4$ . The first number in each box corresponds to  $\omega_r$  and the second to  $\omega_i$ .

$\frac{K_z}{M}$	0.1	0.2	0.5	0.75	1.0
10	0.0018	0.00666	0.0124155	0.02484	0.03312
	0.00236	0.003914	0.002815	0.00651	0.007683
8	0.000215	0.00904	0.0284	0.044535	0.05997
	0.002279	0.00862	0.0064	0.0062025	0.00702
6	0.000048	0	0.019825	0.0356025	0.04782
	0.00102	0.02836	0.00535	0.00361425	0.00338
4	0.003821		0.022125	0	0.01998
	0.001379		0.0072	0.0075	0.00392
2	0		0		0.00279
	0		0		0

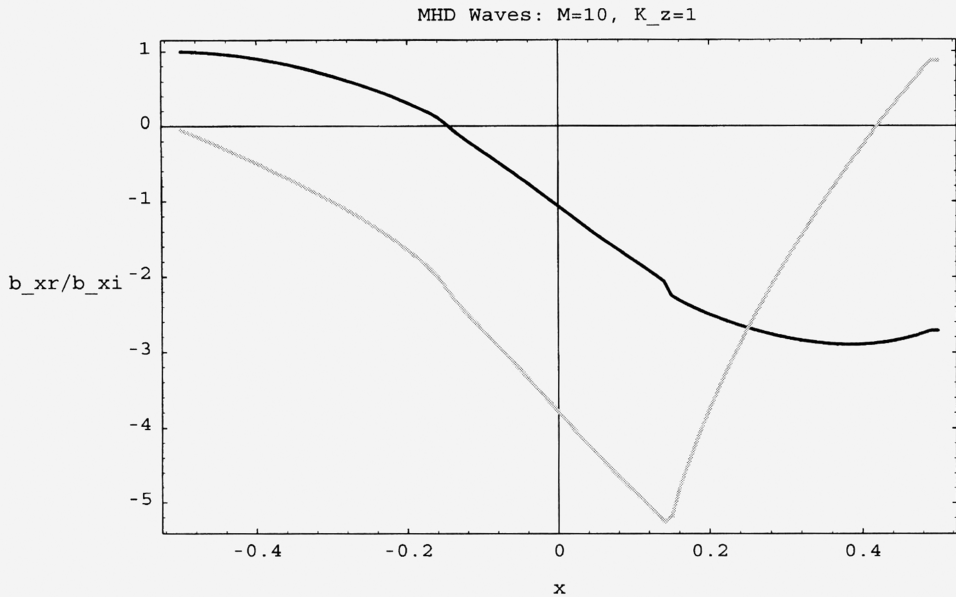


FIG. 8. Real (dark) and imaginary (light) parts of  $\delta b_x$  for the MHD case with  $M = 10$  and  $K_z = 1$  and with  $q_D = 1$  and  $r = 2$ . For this case,  $\omega = 0.03312 + i0.007683$  in units of  $(S_\perp/L)$ ;  $k_- = 4.205 + i0.00659$ ; and  $k_+ = 4.163 - i0.00664$  in units of  $(1/L)$ .

Figure 8 shows the  $\delta b_{xr}$  and  $\delta b_{xi}$  profiles for an unstable mode of the MHD case with  $M = 10$  and  $K_z = 1$  with  $q_D = 1$  and  $r = 2$ . Once again, we can see that there is a resonant layer at the kink,  $\bar{x}_* \approx 0.14$ . The  $k_{x\pm}$  values are approximately 4 in units of  $(1/L)$ , while  $k_z$  has the value 1. Hence, once again, the magnitudes of the  $x$  and  $z$  wavenumbers are comparable.

The weak instability and large regimes of stability in Tables 3 and 4 are due to the high value of  $q_D$  that was used. If the value is reduced, the stability of these two cases is reduced and stronger instability is found.

With this most general case we are able to examine cases that have not been looked at previously. For example, the isothermal waves and the mixed waves have not been considered prior to this. Since the procedure of solving was performed with generalized polytrope indices, we are able to set them as we wish and get results for any case. This allows us to compare and contrast many different cases without having to resolve the governing equations for each case.

If we compare Table 1, the table for the isothermal wave case, and Table 2, the table for the mixed wave case, we can see that the strongest instability in both cases occurs at or about  $M = 10$ . The growth rates grow as  $K_z$  is increased in both cases. These two cases both have the strongest instability at short wavelengths.

In Table 3, the table for the CGL case, the instability along the Mach number slice  $M = 10$ , while quite weak, has a maximum at  $K_z = 0.1$ , which indicates that the instability occurs at long wavelengths. This is in contrast to the results in Tables 1 and 2, the tables for isothermal waves and mixed waves respectively, as noted above.

In Table 4, the table for the MHD case, the growth rate along the slice  $M = 10$  has a maximum at  $K_z = 1.0$ , which indicates that the strongest instability is again at short wavelengths. This is consistent with Tables 1 and 2, the tables for isothermal waves and mixed waves respectively, but is in contrast to Table 3, the table for the CGL case.

It is well known that linear profiles lead to roots that change character when smoother functions like  $\tanh$  are used. For the Rayleigh equation, a linear profile leads to a neutral mode for large  $K_z$ , while a  $\tanh$  profile leads to a more physical damped root for similar values of  $K_z$ . For isotropic shear layers, this kind of behavior is not present. Fluid dynamic shear layers having hyperbolic tangent [12]–[13] and sinusoidal [14] velocity profiles exhibit very similar behavior to linear profile layers. The contours of constant growth rate are somewhat more complex in detail. However, the structure of both the unstable standing and traveling wave modes is similar for these profiles (having nonzero second and higher derivatives of the velocity) to that for linear velocity profile shear layers. These comments remain valid for the present, anisotropic case. We have verified the presence of the unstable standing and traveling wave modes in all ranges of  $K_z$  and  $M$  for a double adiabatic shear layer having a hyperbolic tangent profile. The shooting numerical technique of Sec. 5 is employed. However, the detailed mode structure has not been computed for this case.

In conclusion, we find that the instability of a supersonic/super-Alfvénic anisotropic shear layer, caused by the nonlocal coupling of the generalized firehose and mirror modes by a spatially varying velocity, is very different from the instability of an anisotropic vortex sheet. The structure of the unstable modes in the  $(K_z, M)$ -plane is somewhat different for the cases with  $r = 2$  and  $r = 4$ . The criteria for traveling and standing unstable modes for the anisotropic vortex sheet represented by Eqs. (15) and (22) no longer apply. Unstable traveling and standing wave modes occur at all values of the Mach number. Hence, the second layer is linearly unstable everywhere in the  $(K_z, M)$ -plane (for  $M \leq 15$  and  $K_z \leq 5$ ) with the fastest growing modes occurring at short wavelengths. The instability also differs in structure from that of an isotropic, magnetized shear layer [14]. There the growth rates are smaller for both standing and traveling wave modes. Also, for the anisotropic shear layer, standing wave modes occur everywhere in the  $(K_z, M)$ -plane. For isotropic shear layers, standing wave modes exist only at long wavelengths and small values of the Mach number.

## REFERENCES

- [1] A. K. Sen, *Stability of the magnetosphere boundary*, Planetary and Space Science **13**, 131–141 (1965)
- [2] J. F. Mckenzie, *Hydromagnetic oscillations of the geomagnetic tail and plasma sheet*, J. Geophysical Res. **75**, 5331–5339 (1970)
- [3] D. J. Southwood, *Some features of the field line resonances in the magnetosphere*, Planetary and Space Science **22**, 483–491 (1974)
- [4] L. Chen and A. Hasegawa, *A theory of long-period magnetic pulsations*, J. Geophysical Res. **79**, 1024–1032 (1974)
- [5] F. L. Scarf, W. S. Kurth, D. A. Gurnett, H. S. Bridge, and J. D. Sullivan, *Jupiter tail phenomena upstream from Saturn*, Nature **292**, 585–586 (1981)
- [6] H. Dobrowolny and N. D’Angelo, *Wave motion in type I comet tails*, in *Cosmic Plasma Physics* (K. Schindler, ed.), Plenum Press, New York, 1972

- [7] A. I. Ershkovich, A. A. Nusnov, and A. A. Chernikov, *Oscillations of type I comet tails*, Planetary and Space Science **20**, 1235–1243 (1972); and, *Nonlinear waves in type I comet tails* **21**, 663–673 (1973)
- [8] B. D. Turland and P. A. G. Scheuer, *Instabilities of Kelvin-Helmholtz type for relativistic streaming*, Monthly Notices Roy. Astron. Soc. **176**, 421–441 (1976)
- [9] R. D. Blandford and J. E. Pringle, *Kelvin-Helmholtz instability of relativistic beams*, Monthly Notices Roy. Astron. Soc. **176**, 443–454 (1976)
- [10] S. Chandrasekhar, *Hydrodynamic and Hydromagnetic Stability*, Dover (originally published 1961, Oxford, Clarendon), New York, 1981; A. Syrovatskii, *The Helmholtz instability*, Soviet Physics Uspekhi **62**, 247–253 (1957); T. G. Northrop, *Helmholtz instability of a plasma*, Physical Review (Second series) **103**, 1150–1154 (1956)
- [11] R. A. Gerwin, *Stability of the interface between two fluids in relative motion*, Rev. Modern Phys. **40**, 652–658 (1968)
- [12] T. P. Ray and A. I. Ershkovich, *Kelvin-Helmholtz instabilities of magnetized shear layers*, Monthly Notices Roy. Astron. Soc. **204**, 821–826 (1983)
- [13] A. Miura, *Anomalous transport by magnetohydrodynamic Kelvin-Helmholtz instabilities in the solar wind-magnetosphere interaction*, J. Geophysical Res. **89**, 801–818 (1984)
- [14] S. Roy Choudhury and R. V. Lovelace, *On the Kelvin-Helmholtz instabilities of supersonic shear layers*, Astrophysical J. **283**, 331–342 (1984); and, *On the Kelvin-Helmholtz instabilities of high-velocity magnetized shear layers* **302**, 188–199 (1986); A. Miura and P. L. Pritchett, *Nonlinear stability analysis of the MHD Kelvin-Helmholtz instability in a compressible plasma*, J. Geophysical Res. **87**, 7431–7444 (1982)
- [15] S. Roy Choudhury, *Kelvin-Helmholtz instabilities of supersonic, magnetized shear layers*, J. Plasma Phys. **35**, 375–392 (1986)
- [16] C. Uberoi, *On the Kelvin-Helmholtz instabilities of structured plasma layers in the magnetosphere*, Planetary and Space Science **34**, 1223–1227 (1986)
- [17] M. Fujimota and T. Terasawa, *Ion inertia effect on the Kelvin-Helmholtz instability*, J. Geophysical Res. **96**, 15725–15734 (1991)
- [18] A. C. Sharma and K. M. Shrivastava, *Magnetospheric plasma waves*, Astrophys. Space Sci. **200**, 107–115 (1993)
- [19] S. K. Malik and M. Singh, *Chaos in Kelvin-Helmholtz instability in magnetic fluids*, Phys. Fluids A **4**, 2915–2922 (1992)
- [20] S. Roy Choudhury and V. L. Patel, *Kelvin-Helmholtz instabilities of high-velocity, magnetized anisotropic shear layers*, Phys. Fluids **28**, 3292–3301 (1985)
- [21] S. Duhau, F. Gratton, and J. Gratton, *Hydromagnetic oscillations of a tangential discontinuity in the CGL approximation*, Phys. Fluids **13**, 1503–1509 (1970)
- [22] S. Duhau, F. Gratton, and J. Gratton, *Radiation of hydromagnetic waves from a tangential velocity discontinuity*, Phys. Fluids **14**, 2067–2071 (1971)
- [23] S. Duhau and J. Gratton, *Effect of compressibility on the stability of a vortex sheet in an ideal magneto-fluid*, Phys. Fluids **16**, 150–152 (1972)
- [24] R. Rajaram, G. L. Kalra, and J. N. Tandon, *Discontinuities and the magnetospheric phenomena*, J. Atmos. Terr. Phys. **40**, 991–1000 (1978)
- [25] R. Rajaram, G. L. Kalra, and J. N. Tandon, *Discontinuities in the magnetosphere*, Astrophys. Space Sci. **67**, 137–150 (1980)
- [26] S. P. Talwar, *Hydromagnetic stability of the magnetospheric boundary*, J. Geophysical Res. **69**, 2707–2713 (1964)
- [27] S. P. Talwar, *Kelvin-Helmholtz instability in an anisotropic plasma*, Phys. Fluids **8**, 1295–1299 (1965)
- [28] Zu-Yin Pu, *Kelvin-Helmholtz instability in collisionless space plasmas*, Phys. Fluids B **1**, 440–447 (1989)
- [29] B. A. Shrauner, *Small amplitude hydromagnetic waves for a plasma with a generalized polytropic law*, Plasma Phys. **15**, 375–385 (1973)
- [30] S. Roy Choudhury, *An analytical study of the Kelvin-Helmholtz instabilities of compressible, magnetized anisotropic tangential velocity discontinuities*, Phys. Fluids **29**, 1509–1519 (1986)
- [31] S. Roy Choudhury, *Global asymptotic analysis of the Kelvin-Helmholtz instability of supersonic shear layers*, Canadian J. Physics **68**, 334–342 (1990)